# Analysis of Grid Fins for Launch Abort Vehicle Using a Cartesian Euler Solver

James E. Kless* and Michael J. Aftosmis†

*NASA Ames Research Center, MS 258-2 Moffett Field, CA 94035*

**This paper conducts a numerical study of four sets of aerodynamic control surfaces, called grid fins, mounted on a full Launch Abort Vehicle geometry using a Cartesian Euler Solver with embedded boundaries and adjoint-driven adaptive meshing. Since Cartesian methods are insensitive to complex geometry, this makes them suitable for the highly complex resulting configuration. Numerical results are compared against sub- trans- and supersonic wind tunnel data in order to examine our ability to accurately predict the force and moment increments afforded by these unconventional control surfaces. A database of 1152 separate cases were ran including 12 different Mach numbers from 0.5 - 2.5, 15 different angle of attacks (0 - 15°), and 6 different geometries. Overall, the simulation data show good agreement with tunnel runs and similar rankings of configurations and trends are found between wind tunnel and simulation results suggesting a large potential for Cartesian Euler Solvers in accurately predicting force and moment increments for grid fins on the Launch Abort Vehicle. In particular, pitching moment was predicted accurately over the entire Mach-alpha space.**

## Nomenclature

| | |
|---|---|
| $M_\infty$ | = free-stream mach number |
| $C_A$ | = axial force in missile axis |
| $C_N$ | = normal force in missile axis frame |
| $C_m$ | = pitching moment in missile axis frame (with respect to c.g.) |
| $\alpha$ | = angle of attack, deg |
| $C_P$ | = pressure coefficient |
| $E$ | = total output error in functional value |
| $J$ | = functional value |
| $e$ | = relative error in functional value |
| $\psi$ | = adjoint variable |
| $R$ | = Euler residual terms |
| $(+)$ | = circumferential positioning of grid fins. first fin aligned w/ vertical |
| $(\times)$ | = circumferential positioning of grid fins. first fin 45 degrees w/ vertical |
| $LAV$ | = Launch Abort Vehicle |
| $AMs$ | = LAV abort motors |
| $ACMs$ | = attitude control motors |
| $CM$ | = Crew Module |

## I. Introduction

GRID fins, also known as lattice fins, are unconventional aerodynamic control surfaces first proposed by Belotzerkovsky et al.[1] They consist of an outer frame which supports an inner lattice of intersecting

*Aerospace Engineer, Science and Technology Corporation, Hampton, VA., AIAA Member

†Aerospace Engineer, NASA Ames Research Center, CA, AIAA Associate Fellow

planar surfaces or wings of small chord. Unlike planar fins, grid fins are aligned perpendicular to the flow field to allow the air to pass through the lattice of grid cells. The truss structure formed by the lattice fins is inherently strong, which allows the lattice walls to be extremely thin, reducing the weight and cost. One of the main advantages of grid fins is that, due to their shorter chord lengths, at higher speeds, they generate lower hinge moments than planar wings requiring smaller actuators to rotate them. Additionally, the smaller chord and cascade-like flow reduces the likelihood of stall at high angles of attack relative to conventional planar fins offering increased control effectiveness. To this point, grid fins have found numerous uses on missiles and other endeavors.

The relative amounts of drag for both planar and lattice fins is also an important concern with regard to launch abort vehicles. With careful design, grid fins can produce subsonic drag comparable to that of planar fins. This is due to the thin profile of the lattice walls which create very little disturbance in the flow passing through. In the transonic region, shocks can form in the cascade-like fins restricting the flow through the lattice, significantly increasing the drag force. As the Mach number is increased to slightly faster than $M_\infty = 1$, a bow shock wave can form upstream of the grid fins. This bow shock worsens the effect of the choked flow by forcing more of the flow around the fins, effectively acting as an obstacle to the flow and reducing control effectiveness further. At higher supersonic speeds, the normal shock is swallowed and attached shock waves form at the leading edges of the lattice at an oblique angle. As the Mach number is further increased, the shock passes through the structure without intersecting it, resulting in greater control effectiveness (compared to planar fins) in this regime.[2]

It was shown numerically in Zeng, et al.[3] that by using swept back grid fins, the flow choking is reduced. As a result for the Mach number range of 0.817-2.0, at zero angle of attack, it was found that the sweptback grid fins produced 12% lower drag than the unswept grid fins. Debiasi et al.[4] showed similar benefits for drag reduction of fins with sharp leading edges.

The Orion Launch Abort Vehicle (LAV) is a tower mounted tractor rocket, designed to carry the Crew Module (CM) safely away from the launch vehicle in the unlikely event of a catastrophic failure during launch and ascent. The overall design of the vehicle can be seen in Fig. 1. The primary mechanism for directional control of the vehicle are the eight solid-fueled Attitude Control Motors (ACMs). Since the LAV trajectory includes both nose-forward and heatshield-forward portions of the flight path it is designed with very thin stability margins and a study of deployable grid fins was commissioned.

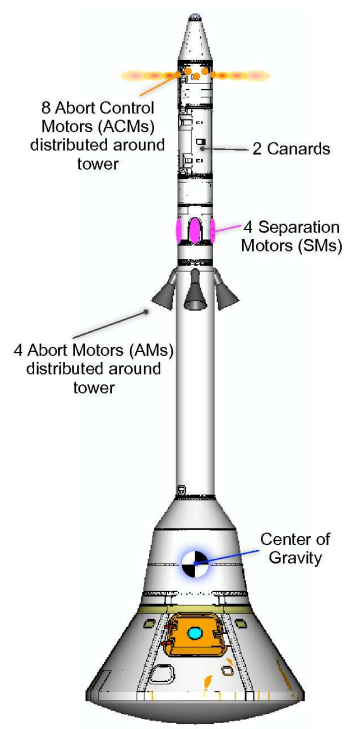


**Figure 1. Schematic Orion LAV**

Since the flow through the lattice structure of grid fins and over the LAV itself is so complex, high-fidelity CFD tools are required to accurately model the flow structure. The main purpose of the current study was to examine the predictive capabilities of NASA's AERO package for these highly complex flows. Adjoint-Based mesh adaptation was used to ensure grid converged solutions optimized for surface loads. In this way, the best possible answer could be computed with a given cell budget. A large matrix of cases were simulated representing a wide range of possible abort scenarios, all advanced to a steady-state solution. The run conditions consisted of a Mach number range of 0.5-2.5 (12 different Mach numbers), an alpha range of $0 - 15°$ (16 total), and 6 different geometries, comprising a total of 1152 separate cases. The geometries simulated included a baseline configuration, two separate circumferential arrangements of unswept grid fins (four fins total), two separate circumferential arrangements of swept fins (four fins total), and a separate case with one isolated unswept grid fin. Loads were computed on 23 separate components of the LAV including many of the components shown in Fig. 1 in addition to hinge moments on the fins. All cases were run on the Columbia and Plaeides Supercomputers at the NASA Advanced Supercomputing Division. The main objective of this investigation was to assess the predictive capability of the Cartesian Euler package for determining aerodynamic load increments as compared to experimental results. While this study is

primarily interested in predicting the grid-fin increments to axial force, normal force and pitching moment, we also investigate the effectiveness of the swept-back fins at reducing drag over the unswept fins, especially transonically and at moderately elevated angles of attack.

# II. Methods

## II.A. Geometry

The geometry used for the study was based on the "26aa" CFD watertight model representation of the Orion LAV shown in Fig. 2. A few of the key components modeled in the geometry include the heatshield, abort motors, feedline (or raceway), and the umbilical notch cutout. These can be found in Fig. 3. As a result of these circumferential asymmetries, the configurations were simulated with no assumptions of symmetry.

A total of six different configurations were studied. The first configuration used the baseline 26aa geometry with no grid fins attached (seen in Fig. 2). The configurations employing the grid fins are shown in Fig. 4. For all the cases, four fins are used which are all spaced at 90 degrees. The (+) configurations align the fins at an offset of 45 degrees with the Abort Motors (AMs) while the (×) configurations align the fins directly aft of the (AMs) in the streamwise direction. Each of the configurations shown was triangulated using $\sim 1.2$ million triangles. The final configuration consisted of one isolated unswept grid fin. This work considers only the unpowered LAV. While power-on experimental data was taken for the fins in the (+) configuration, corresponding data for fins in the (×) orientation was not obtained in the experiment due to high load factors on the grid fins from the Abort Motor jets. Fig. 3 shows a more complete view of the abort motors, raceway, and umbilical notch cutout.

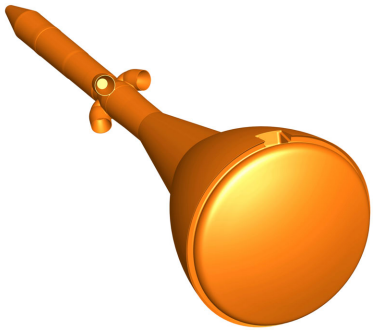

**Figure 2. 26aa LAV baseline configuration (no fins)**

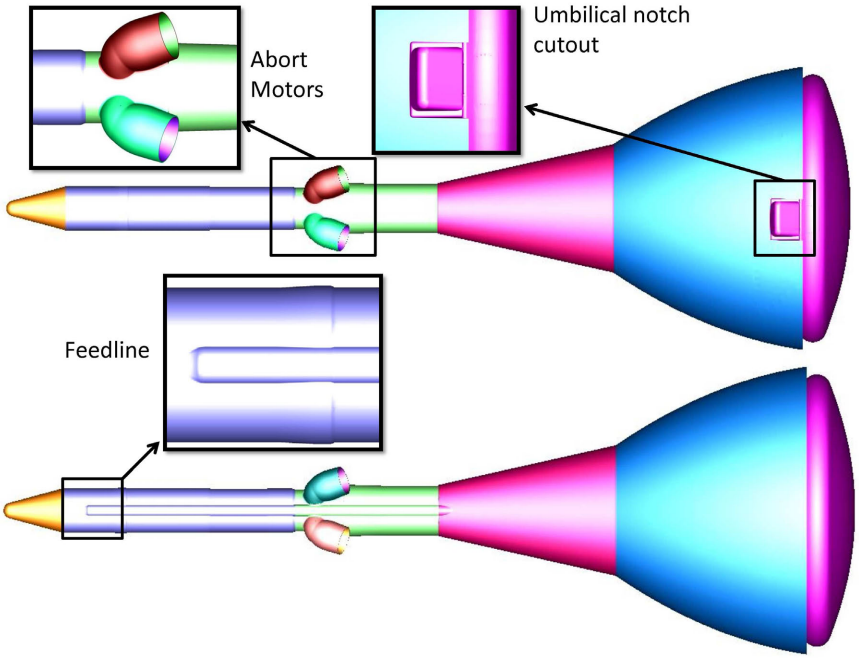


**Figure 3. Baseline 26aa CFD model.**

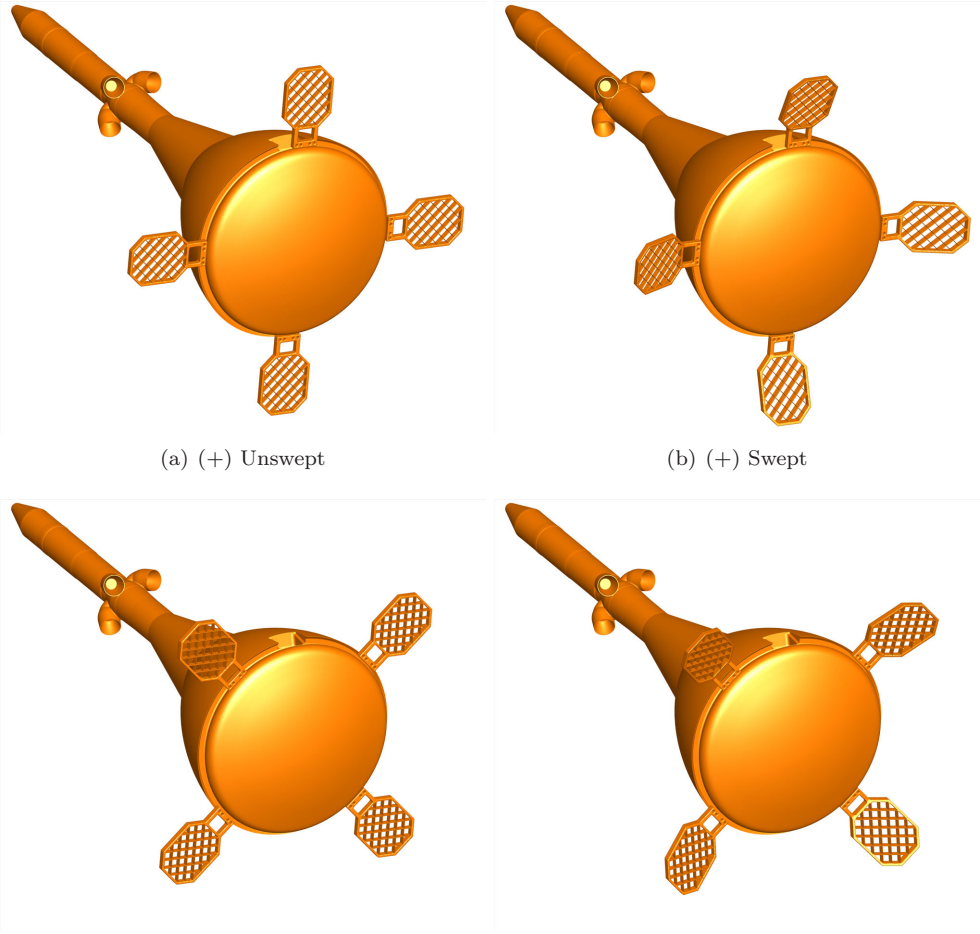

(a) (+) Unswept (b) (+) Swept

(c) (×) Unswept (d) (×) Swept

**Figure 4. LAV grid fins configurations. (a) represents the + configuration with the fins located at the compass points. (b) (+) configuration with 22.5 degree swept grid fins. (c)(×) configuration with 90 degree circumferential spacing and 45 degree offset with from vertical (aligned with the abort motors). (d)(×) configuration with 22.5 degree swept fins.**

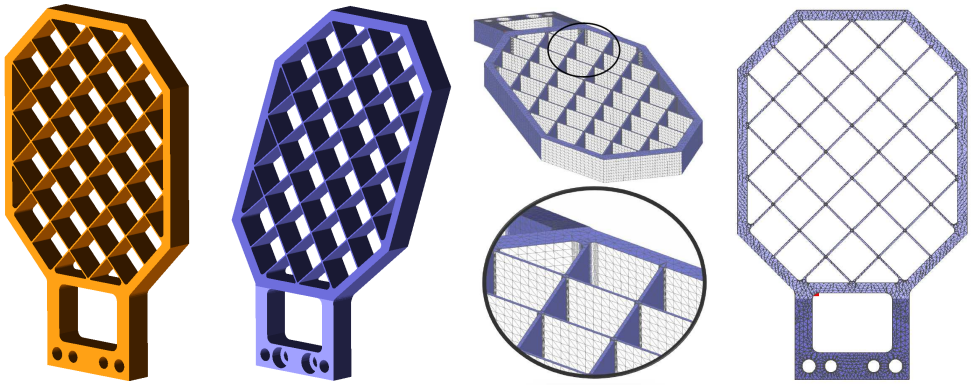

(a) Unswept (b) Swept (c) Triangulation

**Figure 5. Fin geometries considered. (a) CAD model unswept fin. (b) CAD model of swept fin with a sweep angle of 22.5 degrees relative to the unswept fin. (c) representative surface triangulation including $\approx 56,000$ triangles.**

Fig. 5 displays both the swept and unswept CAD models of the fins along with the discretized surface triangulation. The fins were meshed directly from the Pro Engineer CAD parts. However, the baseline

26aa CFD ready triangulation was obtained by first generating an overset mesh grid system on a simplified model, and then, from this using the surface integration tool, Mixsur,[5] to generate a near watertight surface triangulation. Gaps in the Mixsur-outputted Mixsur file were intersected with small geometric shapes to achieve a water-tight geometry. The fins were meshed independently from the LAV baseline 26aa model and subsequently appended to the 26aa without intersecting the aft portion of the LAV. Fig. 3 highlights a few of the geometric details of the 26aa geometry.

### II.B. Flow Solver

NASA's AERO package is a three-dimensional compressible Euler solver suitable for CFD analysis of complex geometries. The AERO package automatically generates an unstructured initial Cartesian volume mesh around the triangulation using an embedded-boundary Cartesian mesh method.[8] This is done by intersecting the triangulation with an initial coarse volume mesh. Cartesian cut-cells are created at the Cartesian mesh/triangulation junction. The treatment of these cut-cells are highlighted in Aftosmis et al.[9] This procedure effectively decouples the surface discretization from the volume mesh, and eliminates the manual labor necessary to generate body-fitted structured meshes. The AERO package then refines this initial coarse mesh in a manner described in the Mesh Adaptation section. The initial surface triangulation is unchanged in all of the mesh refinement studies for all of the cases ran. The complexity of the fin geometry in conjunction with the full LAV make this approach highly appealing.

The simulations for the current study were carried out using second-order, cell-centered, finite-volume scheme with van Leer's flux vector splitting. A multigrid accelerated five-stage Runge-Kutta scheme was used to advance to steady-state. Further details on the numerical aspects and implementation of the AERO package can be found in Aftosmis et al.[10] Domain decomposition provides AERO with essentially linear parallel scalability which allows for fast, automated, aerodynamic database generation. Simulations for a representative case (single Mach number and alpha) were carried out with typically 12-2.9 GHz cores on the Pleiades Supercomputer for $\sim 3-4$ hours for $\sim 6$ million cells. 1152 cases in total were run in parallel over the course of this study. Particular cases that resulted in poor convergence or unusually large discretization errors in the functional were filtered out.

### II.C. Mesh Adaptation

The AERO package has a mesh adaptation module that uses adjoint-weighted residual error estimates to drive mesh adaptation for user selected outputs (such as normal force, axial force, pitching moment, etc.). In this way, the mesh refinement procedure generates a mesh that reduces the discretization errors in the outputs so that the influence of these errors on the output functional is below a specified error tolerance. This meshing strategy is targeted at providing the best possible answer for a given cell budget (or error tolerance).

#### *II.C.1. Error Estimation*

Total error in output functional value, E, can be defined as follows

$$E = J_{exact} - J(Q_H) \tag{1}$$

where $J$ represents the output functional of interest, $Q_H$ is the flow solution satisfying the steady-state three-dimensional Euler equations on mesh of average cell size $H$. Predicting E is difficult to do, even for simple problems. Alternatively, one can estimate how a discrete evaluation of the functional $J(Q_H)$ would change if solved on a finer mesh, h. In this way, a relative error (e) is defined by

$$e = J(Q_h) - J(Q_H) \tag{2}$$

which can be graphically seen in Fig. 6.

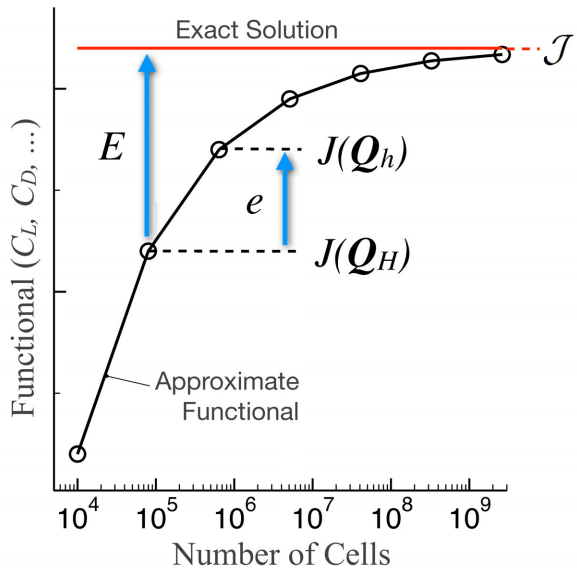


**Figure 6. Discrete estimate of numerical error on a finer mesh of cell-size h**

The goal in the error estimation procedure is to obtain a cell-wise estimate of this relative error ($e(Q_H)$) from the flow solution. Following the development in Nemec et al.,[12] an expression for the functional on the fine mesh can be obtained as a function of the functional on the coarse mesh in terms of the adjoint variable, $\psi$, and the Euler residual terms.

$$J(Q_h) \approx J(Q_H) - \underbrace{(\psi_h^H)^T R(Q_h^H)}_{\text{Adjoint Correction}} - \underbrace{(\psi_h - \psi_h^H)^T R(Q_h^H)}_{\text{Remaining Error}} \tag{3}$$

$Q_h^H$ denotes a reconstruction of the flow solution from the coarse mesh to the fine (embedded) mesh. The remaining error term in equation 3 can be used to determine a bound on the local error in each cell of the embedded mesh.

$$e_k = \mid (\psi_h - \psi_h^H)^T R(Q_h^H) \mid \tag{4}$$

A more complete analysis of the adjoint formulation and its applications on complex geometries can be found in Nemec et al.[6,7]

### *II.C.2. Adaption Strategy*

The mesh refinement process is driven by equation 4. The goal of the adaption strategy is to minimize the cost of the simulation. This is done by gradually increasing the mesh growth factor as the adaption progresses. This approach follows the *Worst things first* strategy of Nemec et al.[7] where the adaption refines cells which contribute the most to error by limiting the mesh growth early on in the refinement. This prevents excessive refinement of coarse meshes when the accuracy of the discrete solution is poor and, in turn, requires only one solution of the flow and adjoint problems on an expensive mesh. As a result, the adaption begins with relatively small growth rates early on and is gradually increased such that the final adaption flags the most amount of cells for refinement and consists of the largest growth.

Most of the cases for the current study consisted of cases that tended to be unsteady and therefore, require large amounts of resolution. The primary culprit for this unsteadiness usually lies in the wake region with moderate error levels. As a result, the *Worst things first* strategy as applied to the current study, refines most of the cells on the pressure side of the vehicle first since they have relatively larger errors early on in the adaption. This avoids over-refinement of the unsteady wake until late in the adaption yielding the best answer for a given cell budget. This strategy has been proven successful for many previous CEV Aerosciences Project reports and used extensively in previous simulations involving complex geometries.

The functional used for the current study is a linear combination of normal force and axial force over the entire model

$$J = C_N + 0.2C_A \tag{5}$$

After experimenting with several functional formulations in Nemec et al.[7] for a similar LAV geometry, it was determined that equation 5 results in good mesh convergence for both forces and moments. Fig. 7 shows the mesh adapted grids for a subsonic and supersonic case.

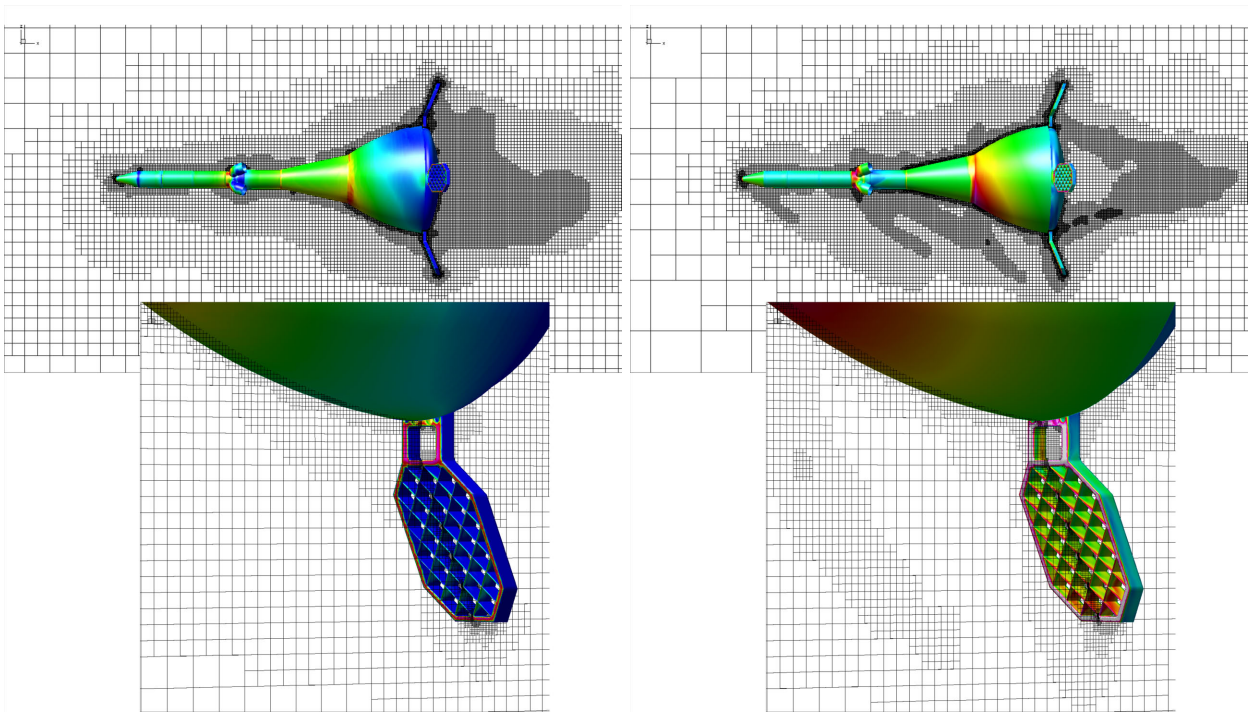

(a) Typical subsonic mesh

(b) Typical supersonic mesh

**Figure 7. Adapted meshes for swept geometry. Fig. (a) shows a typical mesh of 7.6 million cells after 15 adaptation cycles. This case was run at $M_\infty = 0.7$ at $\alpha = 10$ degrees. Fig. (b) shows a typical supersonic case for a typical mesh size of 7.4 million cells and 15 adaptation cycles. This case was simulated at $M_\infty = 1.8$ and $\alpha = 10°$.**

The final refined mesh for the isolated grid fin configuration can be seen in Fig. 8.

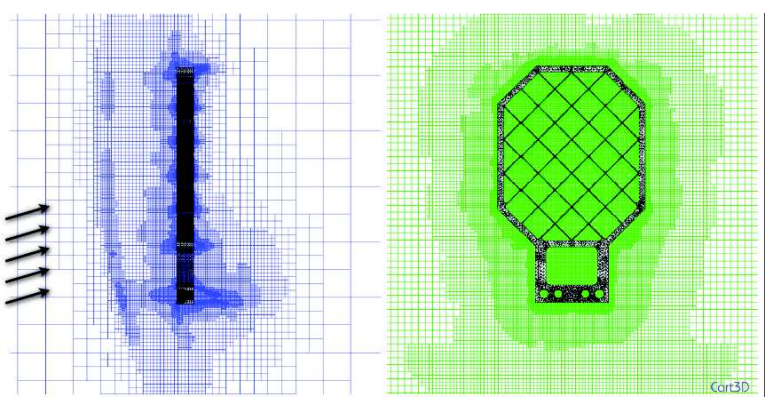


**Figure 8. Fin only configuration; mesh shown after 15 adaptions. $M_\infty = 1.3$, $\alpha = 10$ degrees.**

# III. Results

## III.A. Isolated Grid Fin Results

A single, isolated, unswept grid fin was simulated for 12 different Mach numbers (0.5-2.5) and an alpha range of $0 - 15°$ (16 total). Fig. 9 depicts Mach contours of the singular fin for three different Mach number cases. For the Mach=0.95 case, normal shocks form within the lattice structure creating a large drag rise which can be seen in Fig. 10 (a). As the flow is restricted further in the Mach=1.1 case, the bow shock can be seen in Fig. 9. As the freestream flow is increased further, the shock is swallowed and attached oblique shocks are formed which act to decrease drag. Fig. 10 (b) displays the pitching moments about the base of the grid fin.

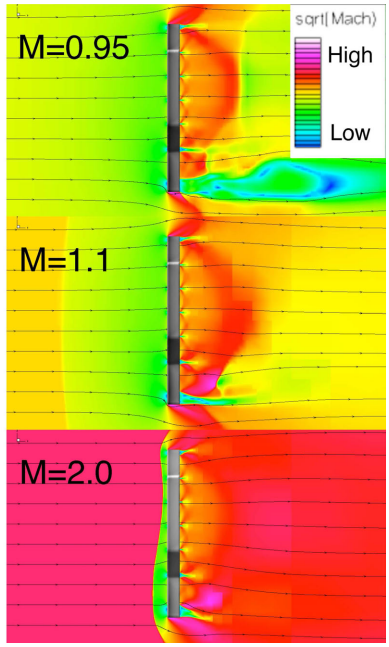


**Figure 9. Isolated grid fin configuration for 3 different Mach numbers all computed at $0°$ angle of attack. The contours are colored by square root of Mach number.**

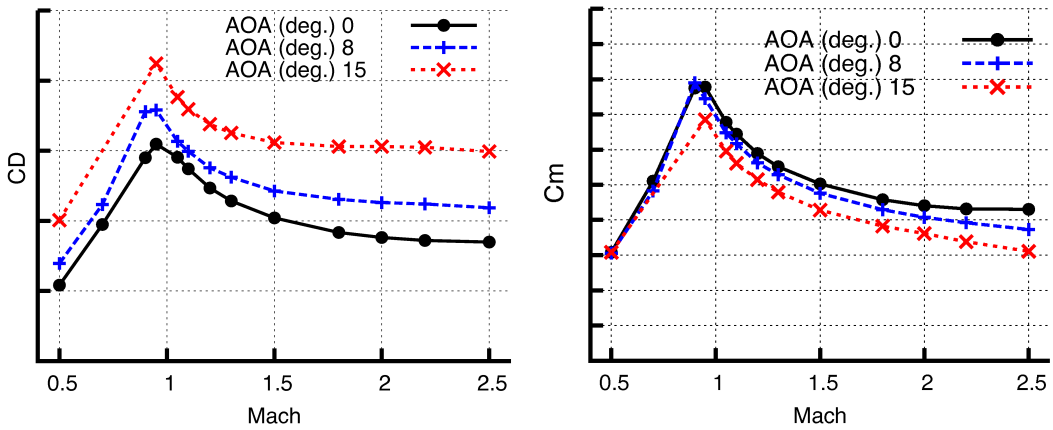


(a) Drag Coefficient

(b) Pitching Moment w.r.t. hinge line

**Figure 10. Single grid fin computations for Drag Coefficient and Pitching Moment Coefficient for $0, 5$, and $15°$ angle of attack. The transonic drag rise due to the flow choking inside the lattice structure can be clearly seen.**

### III.B. Aerodynamic Loads: General Trends

Fig. 11 shows several final meshes of a few cases in the total run matrix along with $C_P$ contours on the surface. Fig. 12 shows mach contours of the same selected run parameters. The final meshes for the runs contained between 7 to 8 million cells. Most of the simulations ran for 10 adaption cycles and all started with the same initial mesh containing 4,000 cells.

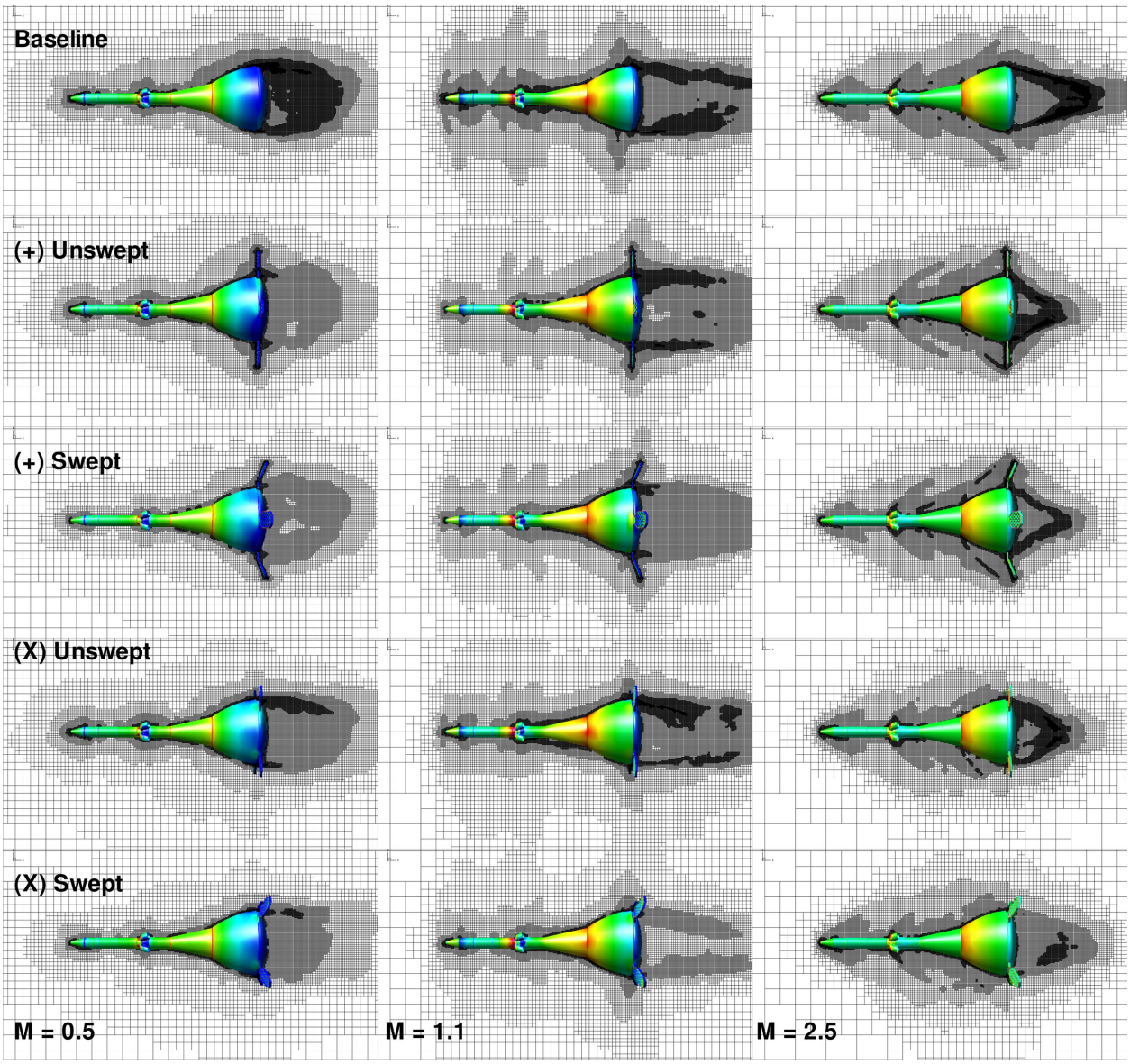


**Figure 11. Final adapted meshes for selected LAV cases. 15 adaptation cycles were used for all cases with each case having $\approx 8$ million cells. surface $C_P$ contours are also shown.**

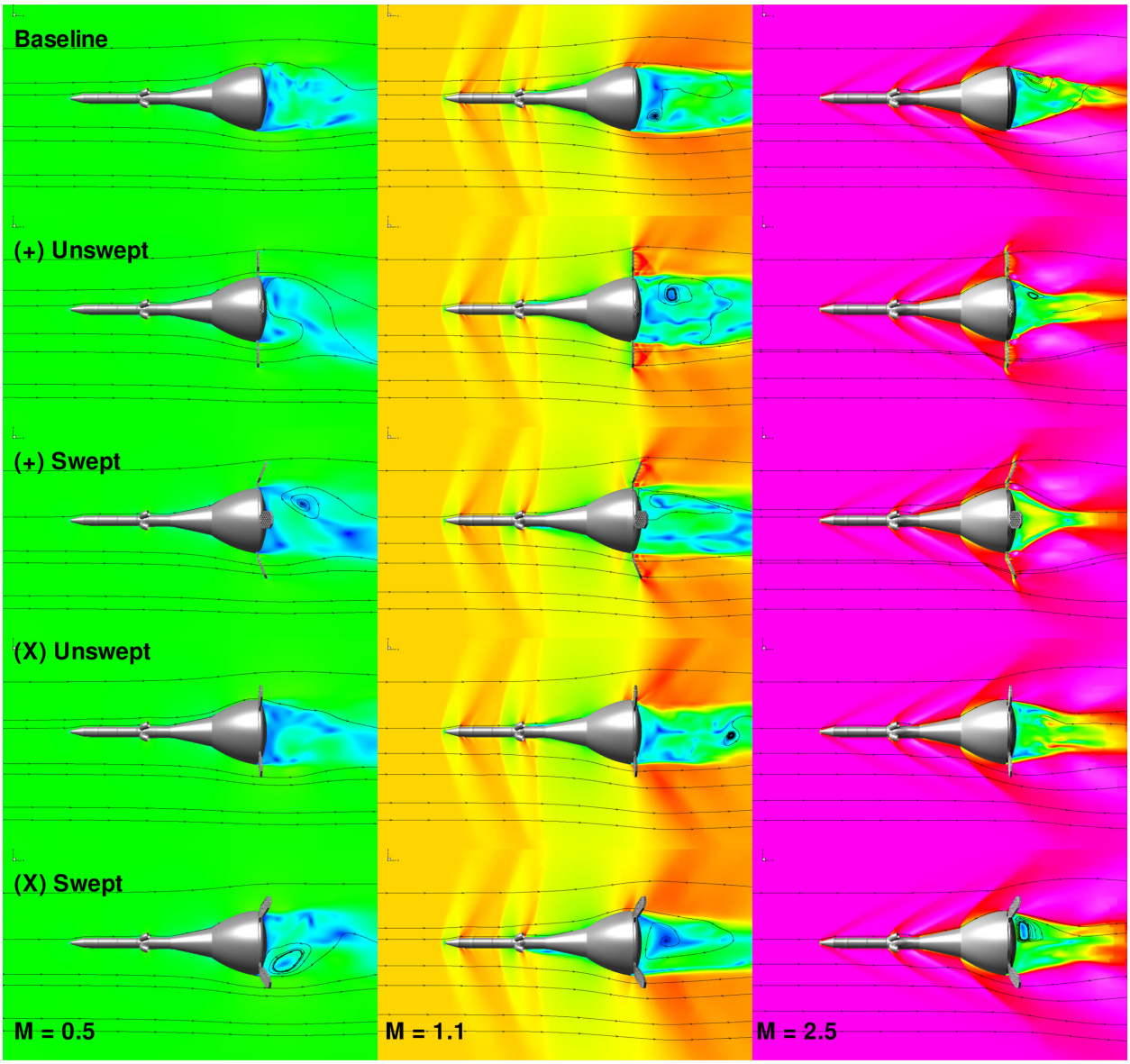


**Figure 12. Mach number contours for selected flow conditions of LAV geometry. The final grids contained between 7 and 8 million cells.**

Fig. 13 displays numerical results for axial force for the 4 configurations at three different flight regimes. The simulation results are shown against the wind tunnel results. Each plot shows a fins on and fins off case. The simulation results over-predict the subsonic and transonic drag rise, both with and without fins present. At higher supersonic mach numbers (not all shown), axial force is predicted accurately by the simulation.

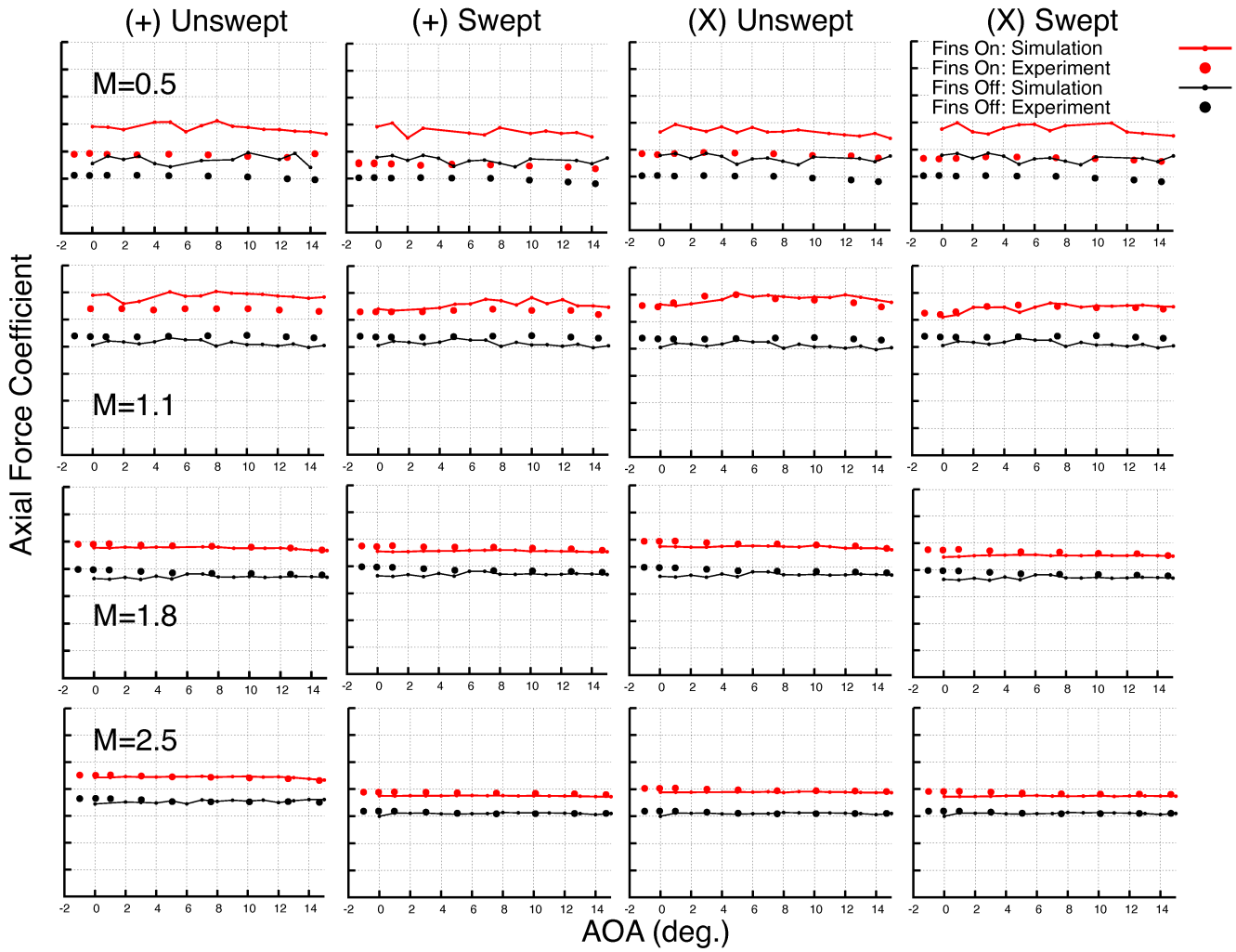


**Figure 13. Axial force coefficients vs. angle of attack for all of the configurations. for the three flight regimes: subsonic, transonic, and supersonic.**

Likewise, simulation results for Normal Force are plotted for the 4 configurations in Fig. 14.

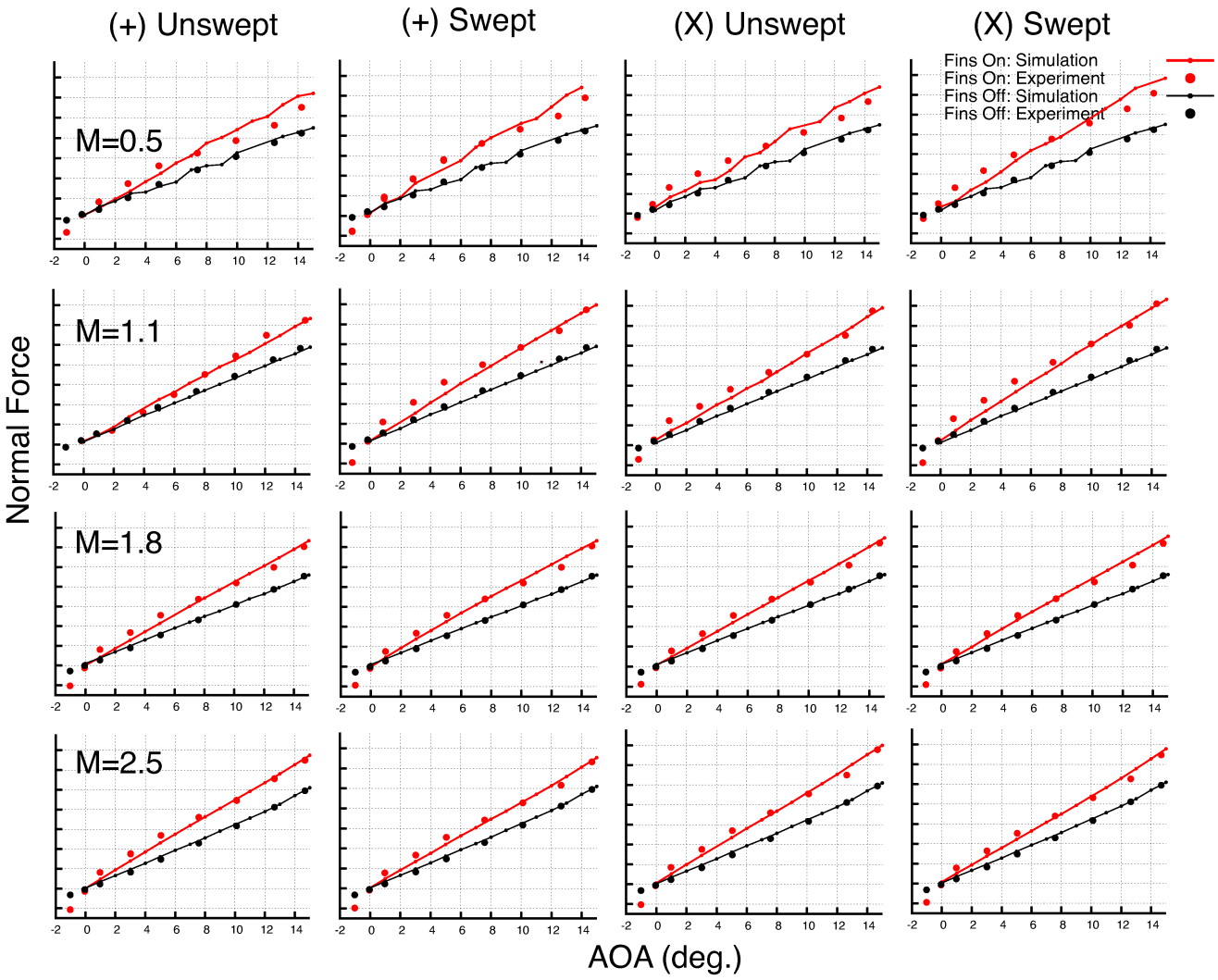


**Figure 14. Normal Force coefficients vs. angle of attack for all of the unswept and swept configurations. The configurations are shown for the three flight regimes: subsonic, transonic, and supersonic.**

Fig. 15 displays baseline (no grid fins) comparisons for normal force, axial force, and pitching moment (about the center of gravity) at 5, and 10 degrees angle of attack. The axial force rise at subsonic and transonic speeds is over-predicted by the CFD results, while at speeds $Mach > 1$, strong agreement is found between CFD and experiment. Normal Force, and Pitching Moment comparisons match over the entire range.

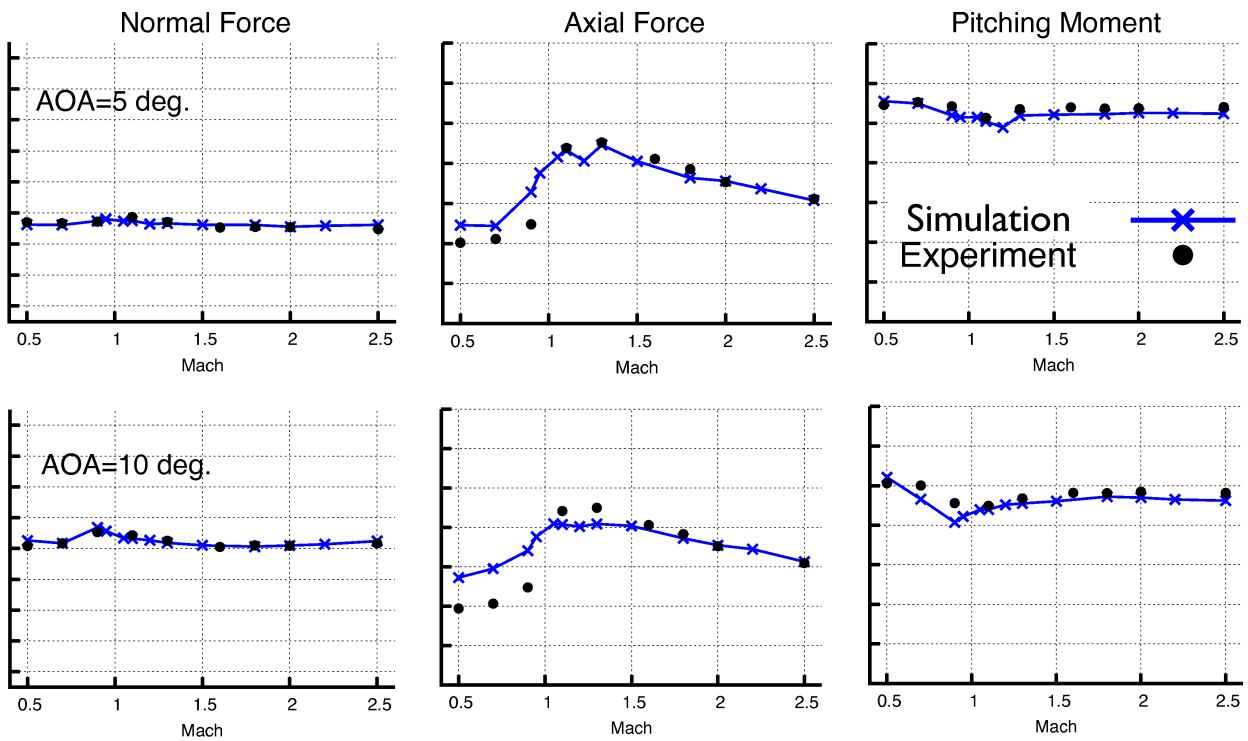


**Figure 15. Baseline 26aa Force coefficients vs. Mach number for 5° and 10° angle of attack. The CFD simulation tends to over-predict axial force in experiment at subsonic speeds. However, strong agreement is seen at supersonic speeds.**

Fig. 18 in the appendix displays axial force and pitching moments for all fin configurations at 10 degrees angle of attack. The over-prediction of axial force for subsonic, and transonic regimes remains consistent across all of the configurations.

Table 1 displays percent differences in flow coefficients between CFD and experiment. The CFD results over-predict axial force. At higher Mach numbers, the axial force differences between the two geometries is reduced. Similar trends are shown for pitching moments. These differences decrease substantially for Mach numbers above 1.

**Table 1. Comparison of Aerodynamic Load differences between the simulation and the wind tunnel data for the baseline configuration with no fins. Tabulated maximum differences from $\alpha = 0 - 15$ degrees. The increments are computed by $100 * ((Simulation - Experiment)/Experiment)$.**

| $M_\infty$ | $\Delta C_A$ | $\Delta C_N$ | $\Delta C_m$ |
|---|---|---|---|
| 0.5 | $\sim 45$ | $< 20$ | $< 16$ |
| 0.7 | $\sim 50$ | $< 4.5$ | $< 20$ |
| 0.9 | $\sim 57$ | $< 6.0$ | $< 23$ |
| 1.1 | $\sim 6.25$ | $< 6.25$ | $< 9.0$ |
| 1.3 | $\sim 11$ | $< 4.5$ | $< 11$ |
| 1.8 | $\sim 6.4$ | $< 11$ | $< 7$ |
| 2.0 | $\sim 4.2$ | $< 8.6$ | $< 30$ |
| 2.5 | $\sim 4.7$ | $< 14$ | $< 27$ |

Pitching moment coefficients are shown in Fig. 16 for the 4 configurations. Improvement is seen between the computational and experimental results. Importantly, the pitching moment increments due to the fins are in good agreement with the experiment.

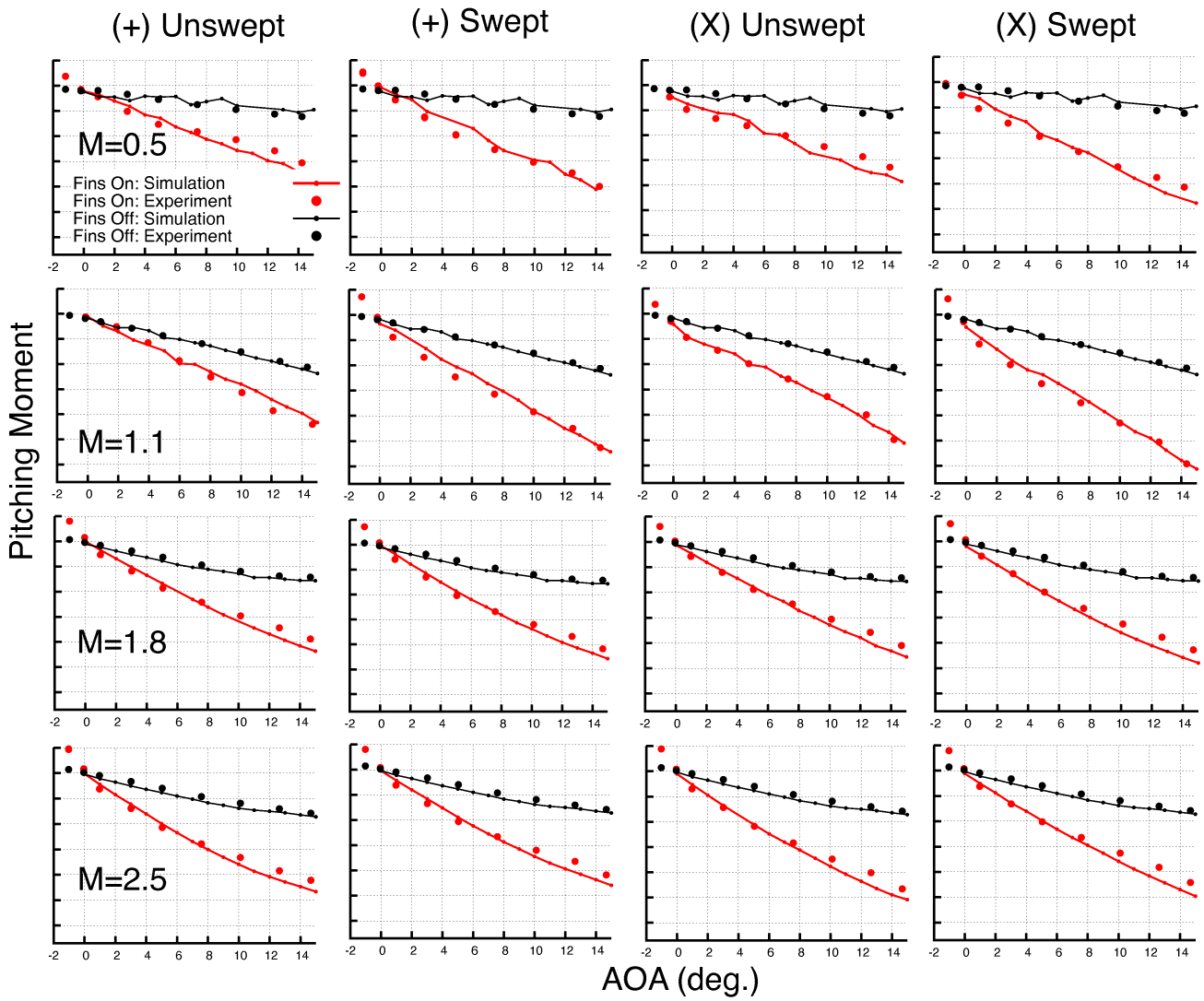


**Figure 16. Pitching moment coefficients vs. angle of attack for all of the configurations. The configurations are shown for the flight regimes: subsonic, transonic, and supersonic.**

### III.C. Fin Stability Augmentation

The total stability augmentation of the fins constituted large benefits in pitching moment at 10 degrees angle of attack. Table 2 gives a complete listing of fin increments in pitching moment at various Mach numbers. The table entries represent the percentage increase in pitching moment for the various configurations.

**Table 2. Simulation prediction of pitching moment increase from baseline (no fins). The entries of the table represent $100 * ((Baseline + fins - Baseline)/Baseline)$ at $\alpha = 10$ degrees.**

| $M_\infty$ | 0.5 | 0.7 | 1.1 | 2.5 |
|---|---|---|---|---|
| (+) unswept | $\sim 224.9$ | $\sim 123.0$ | $\sim 74.5$ | $\sim 160.5$ |
| (+) swept | $\sim 273$ | $\sim 146$ | $\sim 138.5$ | $\sim 149.6$ |
| (×) unswept | $\sim 263$ | $\sim 150$ | $\sim 107.6$ | $\sim 173$ |
| (×) swept | $\sim 332.6$ | $\sim 176$ | $\sim 165.6$ | $\sim 160$ |

Overall, the fins provide between 74 to 330 % increase in pitch. All configurations show a similar trend of maximum pitch increase at Mach = 0.5, a slight decrease in pitch stability in the transonic range, and then a small increase in pitch stability at larger Mach numbers. At subsonic and transonic Mach numbers, the swept fins produce slightly more control stability relative to the unswept fins, while at higher supersonic Mach numbers the benefit is nearly indistinguishable.A similar result is found with regard to the configuration. At the low and transonic Mach numbers, the (×) configuration produces slightly more control authority than the (+) configuration, while at higher Mach numbers the difference is small.

Fig. 17 shows a comparison of experimental and CFD results across a Mach number range of 0.5 to 2.5 at $\alpha = 3°$. The relative rankings of the configurations are the same between both experiment and simulation. Interestingly, in both experiment and simulation, the (×)-swept configuration leads in pitching moment up to $M_\infty = 2.0$, but is overtaken by the (×)-unswept at higher Mach numbers. The pitching moment increase in the transonic range is predicted closely by the AERO package. Over the complete range of Mach numbers, both experiment and CFD simulation predict a slight drag reduction as a result of the swept fins. The benefit seems to diminish at larger Mach numbers.

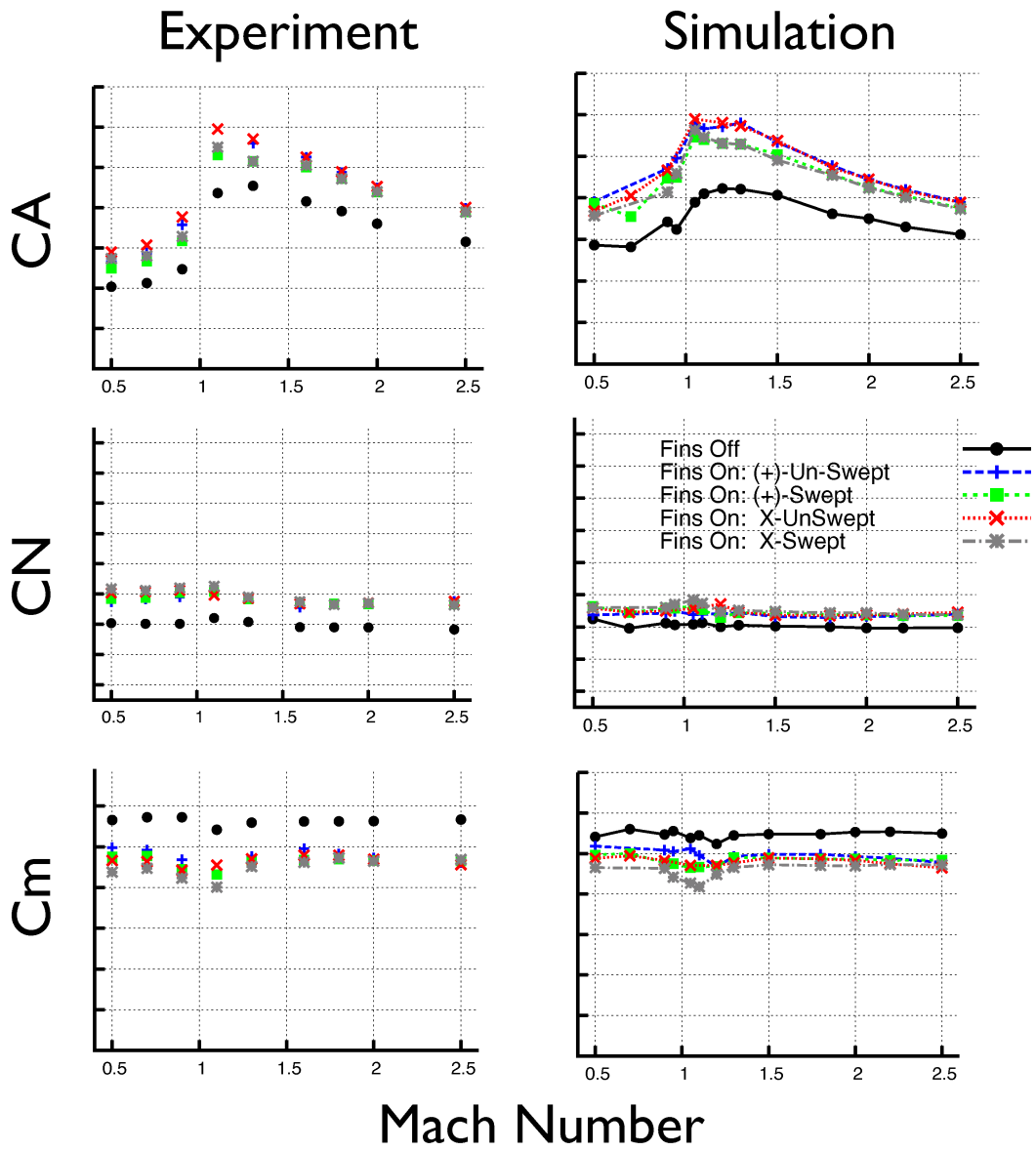


**Figure 17. Pitching moment, Axial Force, and Normal Force coefficients vs. Mach number. Similar increments and consistent rankings among configurations are shown between CFD and experiment for 3° angle of attack.**

### III.D. (+) vs. (×) Configuration

Table 3 summarizes the increments as percentage differences from the baseline configuration due to the different fin configurations for the unswept fin cases at $\alpha = 10°$. The (×) configuration provides slightly more pitch stability with comparable drag margins for the Mach range examined. Table 4 represents this same data for the swept fins.

**Table 3. Simulation prediction of Axial Force, Normal force, and Pitching moment for the unswept fin cases. Increments from baseline (no fins) are shown. The entries of the table represent (Baseline with fins - Baseline) for the case of unswept fins. $\alpha = 10$ degrees.**

| $M_\infty$ | Config | $\Delta C_A$ | $\Delta C_N$ | $\Delta C_m$ |
|---|---|---|---|---|
| 0.5 | (+) | $\sim 35.7$ | $\sim 35.2$ | $\sim 224.9$ |
| | (×) | $\sim 34.4$ | $\sim 43.4$ | $\sim 263$ |
| 0.9 | (+) | $\sim 44.2$ | $\sim 25.4$ | $\sim 60.1$ |
| | (×) | $\sim 35.6$ | $\sim 28.3$ | $\sim 72.9$ |
| 1.1 | (+) | $\sim 46.1$ | $\sim 27.6$ | $\sim 74.5$ |
| | (×) | $\sim 45.2$ | $\sim 39.2$ | $\sim 107.6$ |
| 2.0 | (+) | $\sim 25.9$ | $\sim 38.8$ | $\sim 149.0$ |
| | (×) | $\sim 24.2$ | $\sim 40.5$ | $\sim 160.2$ |
| 2.5 | (+) | $\sim 23.9$ | $\sim 38.7$ | $\sim 160.5$ |
| | (×) | $\sim 25.1$ | $\sim 42.1$ | $\sim 173.3$ |

**Table 4. Simulation prediction of Axial Force, Normal force, and Pitching moment for the swept fin cases. Increments from baseline (no fins) are shown. The entries of the table represent (Baseline with fins - Baseline) for the case of swept fins. $\alpha = 10$ degrees.**

| $M_\infty$ | Config | $\Delta C_A$ | $\Delta C_N$ | $\Delta C_m$ |
|---|---|---|---|---|
| 0.5 | (+) | $\sim 34.5$ | $\sim 41.6$ | $\sim 273$ |
| | (×) | $\sim 35.9$ | $\sim 45.7$ | $\sim 332.6$ |
| 0.9 | (+) | $\sim 26.7$ | $\sim 36.2$ | $\sim 97.3$ |
| | (×) | $\sim 27.9$ | $\sim 40.2$ | $\sim 119.0$ |
| 1.1 | (+) | $\sim 43.0$ | $\sim 44.5$ | $\sim 138.5$ |
| | (×) | $\sim 35.6$ | $\sim 52.2$ | $\sim 165.6$ |
| 2.0 | (+) | $\sim 20.5$ | $\sim 38.8$ | $\sim 159.7$ |
| | (×) | $\sim 19.8$ | $\sim 41.7$ | $\sim 173.1$ |
| 2.5 | (+) | $\sim 19.9$ | $\sim 32.5$ | $\sim 149.6$ |
| | (×) | $\sim 20.2$ | $\sim 35.6$ | $\sim 159.9$ |

For the swept cases, the (×) configuration provides slightly higher stability with comparable axial force values to the (+) configuration.

### III.E. Effect of Swept Fins

Table 5 shows the effect on axial force for both the swept and unswept cases. Consistent with the predictions in Zeng et al.[3] and Debiasi et al.,[4] axial force reductions are seen in the transonic, and to a lesser extent in the low supersonic regime.

**Table 5. AERO prediction of axial force benefit of swept fins for (+) configuration cases. Percentage increments from baseline (no fins) are shown. The entries of the table represent 100*(Baseline with fins - Baseline)/Baseline. $\alpha = 3$ degrees.**

| $M_\infty$ | Sweep | $\Delta C_A$ |
|---|---|---|
| 0.5 | Unswept | $\sim 36.6$ |
| | Swept | $\sim 35.0$ |
| 0.9 | Unswept | $\sim 43.3$ |
| | Swept | $\sim 36.5$ |
| 1.1 | Unswept | $\sim 38.2$ |
| | Swept | $\sim 31.9$ |
| 2.0 | Unswept | $\sim 26.9$ |
| | Swept | $\sim 21.6$ |
| 2.5 | Unswept | $\sim 24.8$ |
| | Swept | $\sim 20.4$ |

Table 6 shows aerodynamic coefficients for the swept and unswept fins for the (+) configuration. For subsonic and transonic regimes, the swept fins provide the highest stability (as measured by pitching moment), while providing lower drag increases than the unswept cases. Similar trends are found in Table 7 for the (×) configuration cases.

**Table 6. Simulation prediction of Axial Force, Normal force, and Pitching moment for (+) configuration cases. Percentage increments from baseline (no fins) are shown. The entries of the table represent 100*((Baseline with fins - Baseline))/Baseline. $\alpha = 10$ degrees.**

| $M_\infty$ | Sweep | $\Delta C_A$ | $\Delta C_N$ | $\Delta C_m$ |
|---|---|---|---|---|
| 0.5 | Unswept | $\sim 35.8$ | $\sim 35.2$ | $\sim 224.9$ |
| | Swept | $\sim 34.6$ | $\sim 41.6$ | $\sim 273.7$ |
| 0.9 | Unswept | $\sim 44.2$ | $\sim 25.4$ | $\sim 60.1$ |
| | Swept | $\sim 26.7$ | $\sim 36.3$ | $\sim 97.4$ |
| 1.1 | Unswept | $\sim 46.1$ | $\sim 27.5$ | $\sim 74.5$ |
| | Swept | $\sim 43.1$ | $\sim 44.5$ | $\sim 138.5$ |
| 2.0 | Unswept | $\sim 25.9$ | $\sim 38.8$ | $\sim 149.0$ |
| | Swept | $\sim 20.5$ | $\sim 38.8$ | $\sim 159.7$ |
| 2.5 | Unswept | $\sim 23.9$ | $\sim 38.7$ | $\sim 160.5$ |
| | Swept | $\sim 19.9$ | $\sim 32.5$ | $\sim 149.6$ |

**Table 7. Simulation prediction of Axial Force, Normal force, and Pitching moment for (×) configuration cases. Percentage increments from baseline (no fins) are shown. The entries of the table represent $100 * (C_{w/fins} - C_{baseline})/C_{baseline}$. $\alpha = 10$ degrees.**

| $M_\infty$ | Sweep | $\Delta C_A$ | $\Delta C_N$ | $\Delta C_m$ |
|---|---|---|---|---|
| 0.5 | Unswept | $\sim 34.5$ | $\sim 43.38$ | $\sim 263.3$ |
| | Swept | $\sim 35.9$ | $\sim 45.7$ | $\sim 332.6$ |
| 0.9 | Unswept | $\sim 35.6$ | $\sim 28.3$ | $\sim 72.9$ |
| | Swept | $\sim 27.9$ | $\sim 40.2$ | $\sim 119.0$ |
| 1.1 | Unswept | $\sim 45.2$ | $\sim 39.2$ | $\sim 107.6$ |
| | Swept | $\sim 35.6$ | $\sim 52.2$ | $\sim 165.6$ |
| 2.0 | Unswept | $\sim 24.2$ | $\sim 40.5$ | $\sim 160.2$ |
| | Swept | $\sim 19.8$ | $\sim 41.7$ | $\sim 173.1$ |
| 2.5 | Unswept | $\sim 25.1$ | $\sim 42.1$ | $\sim 173.3$ |
| | Swept | $\sim 20.2$ | $\sim 35.6$ | $\sim 159.9$ |

# IV. Conclusion

A total of 1152 separate cases were simulated at 12 different Mach numbers from 0.5 - 2.5, 15 different angles of attack from 0 - 15°, and six different configurations using a cut-cell Cartesian grid approach with embedded boundaries. Adjoint-driven mesh refinement was used to provide a grid system optimized for surface loads of interest given a reasonable cell budget. Simulations were generally in good agreement with the wind tunnel data suggesting accurate prediction of the load increments due to the fins using the adjoint-driven grid refinement with less than 8 million cells per case. Similar trends were seen in the transonic regime and the ranking of configurations was consistent. Notably, pitching moment and normal force is in excellent agreement across the database, while axial force is in good agreement to experiment with some tendency to over-predict the experiment in the subsonic regime. Overall, the swept fins show highest pitching moment benefit for both the (+) and (×) configurations in both the simulation and the experiment. Preliminary results show that the (×) configuration provides a slight increase in stability in subsonic and transonic flight. Future studies will need to look at the aerodynamic effect and hinge moments of the plumes impinging upon the fins during LAV powered flight.

# Appendix

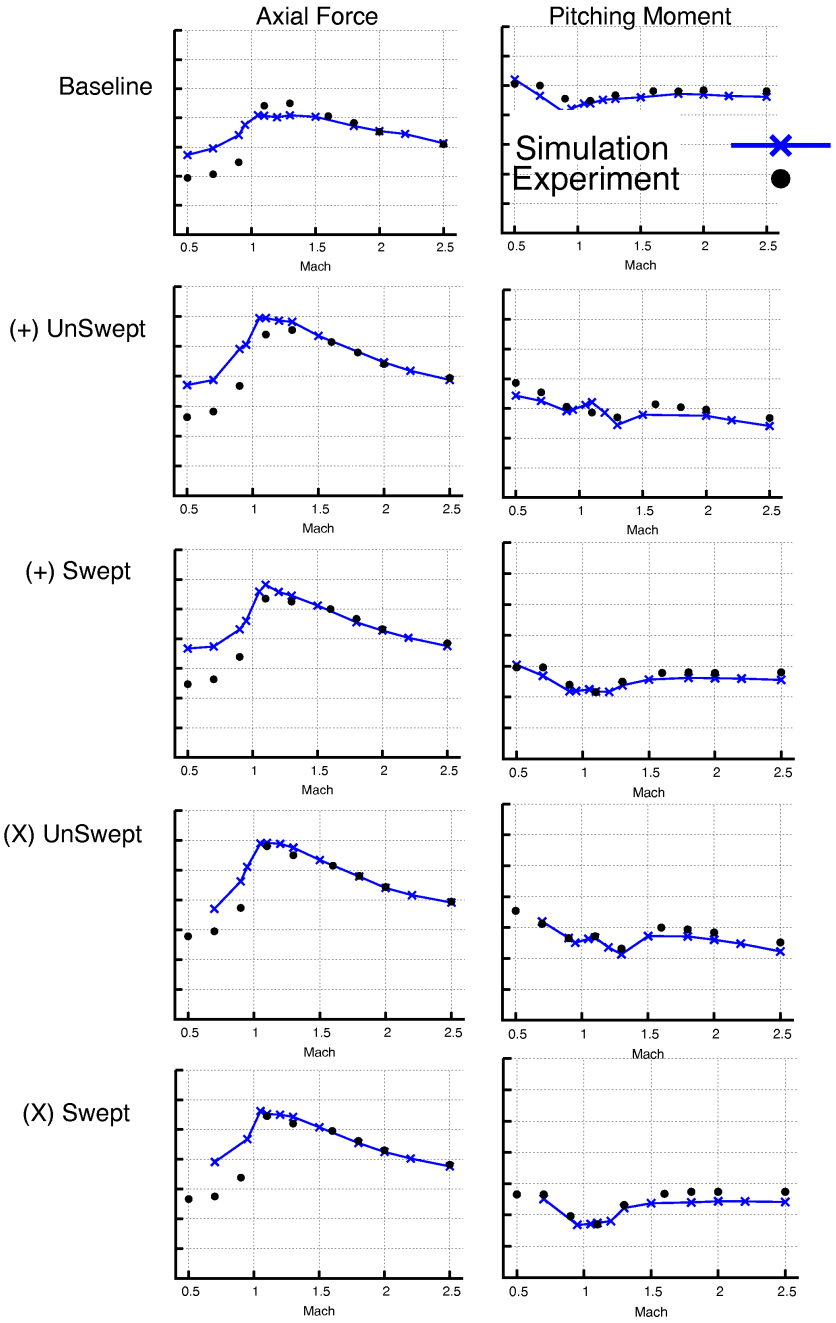


**Figure 18. Force coefficients vs. Mach number. All fin configurations are shown for 10° angle of attack. The over-prediction of axial force for subsonic, and transonic regimes remains consistent across all configurations.**

# Acknowledgments

Special thanks to Michael Mendenhall at Nielson Engineering & Research, Inc. and Reynaldo Gomez at Johnson Space Center for providing the geometry and the wind tunnel data. This work was supported by the NASA Ames Research Center Contract NNA10DF26C.

# References


[1]Belotzerkovsky, S.M.,Odnovol, L. A., Safin, Y. Z., Tyulenev, A. I., Frolov, V. P., and Shitov, V. A., *Reschetchatye Krylya, Moscow, Mashinostroeniye (Russian)*, 1987, (see also: Belotzerkovsky, S.M. et al. *Wings with internal framework*. Machine Translation, FTID(RS)T-1289-89, Foreign Technology Div., 1987).

[2]Orthner, K. S., *Aerodynamic Analysis of Lattice Grids in Transonic Flow*, Master's Thesis, Dept. of Aeronautics and Astronautics, Air Force Institute of Technology, Ohio, 2004.

[3]Zeng, Y., Cai, J., Debiasi, M, Chng, T. L., *Numerical Study on Drag Reduction for Grid-Fin Configurations*, AIAA Paper 2009-1105, 47th AIAA Aerospace Sciences Meeting, Orlando, Florida, Jan 2009.

[4]Debiasi, M, Yan, Z., Loon, C.T., *Swept-back Grid Fins for Transonic Drag Reduction*, AIAA Paper 2010-4244, 28th AIAA Conference, Chicago, Illinois, June, 2010.

[5]Chan, W. M., *Enhancements to the Hybrid Mesh Approach to Surface Loads Integration on Overset Structured Grids*, AIAA Paper 2009–3990, 2009.

[6]Nemec, M., Aftosmis, M.J., Murman, S.M., and Pulliam, T.H., *Adjoint Formulation for an Embedded-Boundary Cartesian Method*, AIAA Paper 2005-0877, 43rd AIAA Aerospace Sciences Meeting, Reno, NV, Jan. 2005. (Also NASA Technical Report NAS-05-008.)

[7]Nemec, M., Aftosmis, M. J., and Wintzer, M., *Adjoint-Based Adaptive Mesh Refinement for Complex Geometries*, AIAA Paper 2008-0725, 46th AIAA Aerospace Sciences Meeting, Reno, NV, Jan 2008.

[8]Aftosmis, M. J., Berger, M.J., *Nemec, Robust and Efficient Cartesian Mesh Generation for Component-Based Geometry* AIAA Journal, 36(6):952-960, June 1998.

[9]Aftosmis, M. J., Berger, M.J., *Adaptive Cartesian Mesh Generation*, Contributed chapter, CRC Handbook of Mesh Generation, 1998.

[10]Aftosmis, M. J., Berger, M.J., *A Parallel Multilevel Method for Adaptively Refined Cartesian Grids with Embedded Boundaries*, AIAA Paper 2000-808, 38th Aerospace Sciences Meeting and Exhibit, Reno, NV, Jan 2000.

[11]Venditti, D. A., and Darmofal, D. L., *Grid Adaptation for Functional Outputs: Application to Two-Dimensional Inviscid Flow*, Journal of Computational Physics, (176);40-69, 2002.

[12]Nemec, M., Aftosmis, M. J., *Adjoint Error Estimation and Adaptive Refinement for Embedded-Boundary Cartesian Meshes*, 18th AIAA Computational Fluid Dynamics Conference, Miami, FL, June 2007